AD-A286 161

ARMY RESEARCH LABORATORY

Application of Chimera Technique
to Projectiles in Relative Motion

Jubaraj Sahu
Charles J. Nietubicz

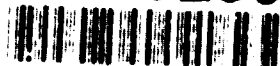ARL-TR-590   October 1994

94-35260

94 11

NOTICES

Destroy this report when it is no longer needed. DO NOT return it to the originator.

Additional copies of this report may be obtained from the National Technical Information Service, U.S. Department of Commerce, 5285 Port Royal Road, Springfield, VA 22161.

The findings of this report are not to be construed as an official Department of the Army position, unless so designated by other authorized documents.

The use of trade names or manufacturers' names in this report does not constitute indorsement of any commercial product.

REPORT DOCUMENTATION PAGE

Form Approved
OMB No. 0704-0188

1. AGENCY USE ONLY (Leave blank)	2. REPORT DATE	3. REPORT TYPE AND DATES COVERED
	October 1994	Final, February 1993 - May 1994

4. TITLE AND SUBTITLE	5. FUNDING NUMBERS
Application of Chimera Technique to Projectiles in Relative Motion	PR: 1L161102AH43 WO: 61102A-00-001-AJ

6. AUTHOR(S)

Jubaraj Sahu and Charles J. Nietubicz

7. PERFORMING ORGANIZATION NAME(S) AND ADDRESS(ES)	8. PERFORMING ORGANIZATION REPORT NUMBER
US Army Research Laboratory ATTN: AMSRL-WT-PB Aberdeen Proving Ground, MD 21005-5066	

9. SPONSORING/MONITORING AGENCY NAMES(S) AND ADDRESS(ES)	10. SPONSORING/MONITORING AGENCY REPORT NUMBER
US Army Research Laboratory ATTN: AMSRL-OP-AP-L Aberdeen Proving Ground, MD 21005-5066	ARL-TR-590

11. SUPPLEMENTARY NOTES

12a. DISTRIBUTION/AVAILABILITY STATEMENT	12b. DISTRIBUTION CODE
Approved for public release; distribution is unlimited.	

13. ABSTRACT (Maximum 200 words)

This report describes the application of the versatile Chimera numerical technique to a time-dependent, multibody projectile configuration. A computational study was performed to determine the aerodynamics of small cylindrical segments being ejected into the wake of a flared projectile. The complexity and uniqueness of this problem results from the segments being in relative motion to each other, embedded in a nonuniform wake flow, and requiring a time-dependent solution. Flow field computations for this multibody problem have been performed for supersonic conditions. The predicted flow field over the segments was found to undergo significant changes as the segments separated from the parent projectile. Comparison of the unsteady Chimera results with the quasi-static approach shows the difference in drag history to be significant which indicates the need for time-dependent solution techniques. A subsequent experimental program was conducted in the Army Research Laboratory's (ARL) Transonic Range and the computed segment positions and velocities were found to be in good agreement with the experimental data.

14. SUBJECT TERMS		15. NUMBER OF PAGES
Aerodynamics; multiple bodies; unsteady flow; Chimera; wake; drag		30
		16. PRICE CODE

17. SECURITY CLASSIFICATION OF REPORT	18. SECURITY CLASSIFICATION OF THIS PAGE	19. SECURITY CLASSIFICATION OF ABSTRACT	20. LIMITATION OF ABSTRACT
UNCLASSIFIED	UNCLASSIFIED	UNCLASSIFIED	SAR

INTENTIONALLY LEFT BLANK.

TABLE OF CONTENTS

INTENTIONALLY LEFT BLANK.

LIST OF FIGURES

INTENTIONALLY LEFT BLANK.

1. INTRODUCTION

An important parameter in the design of shell and bodies flying in relative motion to each other is the total aerodynamic drag. The base drag constitutes a large part of the total aerodynamic drag and accurate prediction of the base region flow field is necessary. The ability to compute the base region flow field for projectile configurations using Navier-Stokes computational techniques has been developed over the past several years.[1,2,3] Recently, improved numerical predictions have been obtained by using the Cray-2 supercomputer and a more advanced zonal upwind flux-split algorithm.[4,5,6] This zonal scheme preserves the geometry of the base corner which allows an accurate modeling of the base region flow. Previous computational studies have been completed showing the aerodynamic effect for a variety of base geometries. These calculations, however, were performed on stand-alone projectile configurations and represent a single-body problem. Recently a multibody problem which involves other bodies flying in the wake of a parent projectile has required computational analyses. This is due in part to the difficulty in finding good experimental and/or analytical data for such problems. The particular problem here is to determine the aerodynamic effect of small cylindrical segments being ejected into the wake of a parent projectile. The complexity and uniqueness of this problem results from the trailing segments being in relative motion to each other, embedded in a non-uniform wake flow, and requiring a time dependent solution. Figure 1 is a spark shadowgraph picture of a recent range test[7] conducted with a number of segments flying in the wake of the parent projectile. Computational results have been obtained by the authors for both the quasi-steady case of fixed positions of the segments in the wake[8] and the dynamic case which involves time-accurate numerical computations and is the subject matter of this technical report.

The time-accurate numerical simulation of the multiple aerodynamic bodies in relative motion has been obtained using the Chimera[9] approach. This technique has been used to compute inviscid and viscous flows about complex configurations,[10,11,12] and has been demonstrated for unsteady viscous flow problems with bodies in relative motion.[13] The Chimera approach is a domain decomposition method which uses overset, body-conforming grids and grew out of the necessity to computationally model geometrically complex configurations. The originally developed Navier-Stokes code, zonal F3D[4], was extended by the authors to include the details of the Chimera procedure. This unique work couples the solution of the Navier-Stokes equations, which govern fluid motion, with the solution to the six DOF (degree-of-freedom) equations of motion.

The coupling of the fluid dynamic solution and rigid body motion is a major advance and a significant accomplishment which eliminates the need for simplifying assumptions and allows more accurate physically based simulations.

2. GOVERNING EQUATIONS AND SOLUTION TECHNIQUE

The complete set of time-dependent, Reynolds-averaged, thin-layer Navier-Stokes equations is solved numerically to obtain a solution to this problem. The numerical technique used is an implicit, finite-difference scheme. Time-accurate calculations are made to numerically simulate the ejection and separation of the segments in the wake of a parent projectile.

2.1 Governing Equations

The complete set of three-dimensional (3-D), time-dependent, generalized geometry, Reynolds-averaged, thin-layer Navier-Stokes equations for general spatial coordinates ξ, η, and ζ can be written as follows:[14]

$$\partial_\tau \hat{q} + \partial_\xi \hat{F} + \partial_\eta \hat{G} + \partial_\zeta \hat{H} = Re^{-1}\partial_\zeta \hat{S} , \tag{1}$$

where

$\xi = \xi(x, y, z, t)$ - longitudinal coordinate;

$\eta = \eta(x, y, z, t)$ - circumferential coordinate

$\zeta = \zeta(x, y, z, t)$ - nearly normal coordinate;

$\tau = t$ - time

and

$$\hat{q} = \frac{1}{J} \begin{bmatrix} \rho \\ \rho u \\ \rho v \\ \rho w \\ e \end{bmatrix} \qquad \hat{F} = \frac{1}{J} \begin{bmatrix} \rho U \\ \rho u U + \xi_x p \\ \rho v U + \xi_y p \\ \rho w U + \xi_z p \\ (e+p)U - \xi_t p \end{bmatrix}$$

$$\hat{G} = \frac{1}{J} \begin{bmatrix} \rho V \\ \rho u V + \eta_x p \\ \rho v V + \eta_y p \\ \rho w V + \eta_z p \\ (e+p)V - \eta_t p \end{bmatrix} \qquad \hat{H} = \frac{1}{J} \begin{bmatrix} \rho W \\ \rho u W + \zeta_x p \\ \rho v W + \zeta_y p \\ \rho w W + \zeta_z p \\ (e+p)W - \zeta_t p \end{bmatrix}$$

(2)

and where

$$\hat{S} = \frac{1}{J} \begin{bmatrix} 0 \\ \mu(\zeta_x^2 + \zeta_y^2 + \zeta_z^2)u_\zeta + \frac{\mu}{3}(\zeta_x u_\zeta + \zeta_y v_\zeta + \zeta_z w_\zeta)\zeta_x \\ \mu(\zeta_x^2 + \zeta_y^2 + \zeta_z^2)v_\zeta + \frac{\mu}{3}(\zeta_x u_\zeta + \zeta_y v_\zeta + \zeta_z w_\zeta)\zeta_y \\ \mu(\zeta_x^2 + \zeta_y^2 + \zeta_z^2)w_\zeta + \frac{\mu}{3}(\zeta_x u_\zeta + \zeta_y v_\zeta + \zeta_z w_\zeta)\zeta_z \\ \left\{ (\zeta_x^2 + \zeta_y^2 + \zeta_z^2)\left[\frac{\mu}{2}(u^2 + v^2 + w^2)_\zeta \right. \right. \\ \left. \left. + \frac{\kappa a_\zeta^2}{Pr(\gamma-1)} \right] \right. \\ \left. + \frac{\mu}{3}(\zeta_x u + \zeta_y v + \zeta_z w)(\zeta_x u_\zeta + \zeta_y v_\zeta + \zeta_z w_\zeta) \right\} \end{bmatrix}$$

(3)

In Equation 1, the thin-layer approximation is used, and the viscous terms involving velocity gradients in both the longitudinal and circumferential directions are neglected. The viscous terms are retained in the normal direction, ζ, for the projectile and segments, and are collected into the vector $\hat{S}$. In the wake or the base region, similar viscous terms are also added in the streamwise direction, ξ. For this computation, the diffusion coefficients μ and κ contain molecular and turbulent parts. The turbulent contributions are supplied through an algebraic eddy viscosity turbulence model developed by Baldwin and Lomax.[15]

The velocities in the ξ, η, and ζ coordinate directions can be written as

$$U = \xi_t + u\xi_x + v\xi_y + w\xi_z$$
$$V = \eta_t + u\eta_x + v\eta_y + w\eta_z$$
$$W = \zeta_t + u\zeta_x + v\zeta_y + w\zeta_z$$

which represent the contravariant velocity components.

The Cartesian velocity components (u, v, w) are retained as the dependent variables and are nondimensionalized with respect to a_∞ (the free-stream speed of sound). The local pressure is determined using the relation

$$p = (\gamma - 1)[e - 0.5\rho(u^2 + v^2 + w^2)] \tag{4}$$

where γ is the ratio of specific heats. Density, ρ, is referenced to ρ_∞ and the total energy, e, to $\rho_\infty a_\infty^2$. The transport coefficients are also nondimensionalized with respect to the corresponding free-stream variables. Thus the Prandtl number which appears in $\hat{S}$ is defined as $Pr = c_{p\infty}\mu_\infty/\kappa_\infty$.

2.2 Numerical Technique

The implicit, approximately factored scheme for the thin-layer Navier-Stokes equations using central differencing in the η and ζ directions and upwinding in ξ is written in the following form,[16]

4

$$\left[I + i_b h \delta_\xi^b (\hat{A}^+)^n + i_b h \delta_\zeta \hat{C}^n - i_b h Re^{-1} \bar{\delta}_\zeta J^{-1} \hat{M}^\eta J - i_b D_i |_\zeta \right]$$

$$\times \left[I + i_b h \delta_\xi' (\hat{A}^-)^n + i_b h \delta_\eta \hat{B}^n - i_b D_i |_\eta \right] \Delta \hat{Q}^\eta$$

$$= -i_b \Delta t \{ \delta_\xi^b [(\hat{F}^+)^n - \hat{F}_-^+] + \delta_\xi' [(\hat{F}^-)^n - \hat{F}_-^-] + \delta_\eta (\hat{G}^n - \hat{G}_-)$$ (6)

$$+ \delta_\zeta (\hat{H}^n - \hat{H}_-) - Re^{-1} \bar{\delta}_\zeta (\hat{S}^n - \hat{S}_-) \} - i_b D_e (\hat{Q}^n - \hat{Q}_-)$$

where $h = \Delta t$ or $(\Delta t)/2$ and the free-stream base solution is used. Here, δ is typically a three-point second-order accurate central difference operator, $\bar{\delta}$ is a midpoint operator used with the viscous terms, and the operators δ_ξ^b and δ_ξ' are backward and forward three-point difference operators. The flux $\hat{F}$ has been eigensplit and the matrices $\hat{A}$, $\hat{B}$, $\hat{C}$, and $\hat{M}$ result from local linearization of the fluxes about the previous time level. Here, J denotes the Jacobian of the coordinate transformation. Dissipation operators D_e and D_i are used in the central space differencing directions. The smoothing terms used in the present study are of the form:

$$D_e |_\eta = (\Delta t) J^{-1} \left[\varepsilon_2 \bar{\delta} \rho (B) \beta \bar{\delta} + \varepsilon_4 \bar{\delta} \frac{\rho(B)}{1+\beta} \bar{\delta}^3 \right] |_\eta J$$

$$D_i |_\eta = (\Delta t) J^{-1} \left[\varepsilon_2 \bar{\delta} \rho (B) \beta \bar{\delta} + 2.5 \varepsilon_4 \bar{\delta} \rho(B) \bar{\delta} \right] |_\eta J$$

where

$$\beta = \frac{|\bar{\delta}^2 P|}{|(1 + \delta^2) P|}$$

and where $\rho(B)$ is the true spectral radius of B. The idea here is that the fourth difference will be tuned down near shocks (e.g., as β gets large, the weight on the fourth difference drops down while the second difference tunes up).

5

2.3 Chimera Composite Grid Scheme

The Chimera overset grid scheme is a domain decomposition approach where a configuration is meshed using a collection of overset grids. It allows each component of the configuration to be gridded separately and overset into a main grid. Overset grids are not required to join in any special way. Usually there is a major grid which covers the entire domain or a grid generated about a dominant body. Minor grids are generated about the rest of the other bodies. Because each component grid is generated independently, portions of one grid may be found to lie within the solid boundary contained within another grid. Such points lie outside the computational domain and are excluded from the solution process.

Figures 2 and 3 show an example where the parent projectile grid is a major grid and the segment grid is a minor grid. The segment grid is completely overlapped by the projectile grid; thus, its outer boundary can obtain information by interpolation from the projectile grid. Similar data transfer or communication is needed from the segment grid to the projectile grid. However, a natural outer boundary that overlaps the segment grid does not exist for the projectile grid. The Chimera technique creates an artificial boundary (also known as a hole boundary) within the projectile grid which provides the required path for information transfer from the segment grid to the projectile grid. The resulting hole region is excluded from the flow field solution in the projectile grid. Equation 5 has been modified for Chimera overset grids by the introduction of the flag i_b to achieve just that. This i_b array accommodates the possibility of having arbitrary holes in the grid. The i_b array is defined such that $i_b = 1$ at normal grid points and $i_b = 0$ at hole points. Thus, when $i_b = 1$, Equation 5 becomes the standard scheme. But, when $i_b = 0$, the algorithm reduces to $\Delta \hat{Q}^n = 0$ or $\hat{Q}^{n+1} = \hat{Q}^n$, leaving $\hat{Q}$ unchanged at hole points. The set of grid points which form the border between the hole points and the normal field points are called intergrid boundary points. These points are updated by interpolating the solution from the overset grid that created the hole. Values of the i_b array and the interpolation coefficients needed for this update are provided by a separate algorithm.[11]

In the present study, which involves multiple bodies in relative motion, the location of the holes and the intergrid boundary points are time-dependent. Accordingly, the i_b array and the interpolation coefficients are functions of time. This procedure of unsteady Chimera decomposition has been successfully demonstrated by Meakin.[13] The method depends on three

functions: domain connectivity, aerodynamics, and body dynamics. The aerodynamics code depends on the domain connectivity code to supply hole and interpolation information. The domain connectivity code, in turn, depends on the body dynamics code to supply the location and orientation of the moving bodies relative to the primary body. Finally, the body dynamics code depends on the aerodynamics code to provide the aerodynamic forces and moments acting on the moving bodies.

The Chimera procedure reduces a complex multibody problem into a number of simpler subproblems. For moving body problems, all grids are allowed to move with six degrees of freedom relative to an inertial reference frame. Accordingly, bodies can move with respect to others without the necessity of generating new grids. With this composite overset grid approach, it is thus possible to determine the unsteady relative motion of the segments and associated aerodynamic forces without the need for costly regridding. This also eliminates potential accuracy problems due to severe grid stretching used by many other techniques. The solution procedure is to compute the flow field at each time step; integrate the pressure and viscous forces for the trailing segments to obtain the drag force; use the predicted drag in a coupled six DOF program to compute the new relative position of the trailing segment. At the next time step, the solution procedure is repeated for the new position with the domain decomposition providing all the required interpolation information. Computations are performed on each grid separately. These grids use the available core memory one grid at a time. The remaining grids are stored on an external disk storage device such as the solid-state disk device (SSD) of the Cray X-MP or Y-MP computer.

2.4 Domain Connectivity Function

A major part of the Chimera overset grid approach is the information transfer from one grid into another by means of the intergrid boundary points. Again, these points consist of a set of points which define the hole boundaries and outer boundaries of the minor grids. These points depend on the solutions in the overlapping regions. In the present work, the Domain Connectivity Function in Three-Dimensions (DCF3D) Code[13] has been used to establish the linkages between the various grids that are required by the flow solver or aerodynamics code described earlier. These include the determination of the interpolation coefficients, and the setting up of Chimera logic for bodies making holes in overlapping grids. For unsteady moving grid cases, this code

7

must be executed at each time iteration. To minimize the computation time, this code uses the knowledge of hole and interpolated boundary points at time level n to limit its search regions for finding their corresponding locations at time level n+1.

In general, each component grid in an overset grid system represents a curvilinear system of points. However, the position of all points in all the grids are defined relative to an inertial system of reference. To provide domain connectivity, inverse mappings are used which allow easy conversion from x,y,z inertial system to ξ,ζ,η computational space. For moving body problems, these maps for component grids are created only once. Identification of the intergrid boundary points which correspond to the outer boundaries of the minor grids are done simply by specifying appropriate ranges of coordinate indices. The rest of the intergrid boundary points which result from holes created by a body in overset grids is a little more difficult to identify. A collection of analytical shapes such as cones, cylinders, and boxes are used to cut holes in this method.

2.5 Boundary Conditions

For simplicity, most of the boundary conditions have been imposed explicitly.[3] An adiabatic wall boundary condition is used on the body surface, and the no-slip boundary condition is used at the wall. The pressure at the wall is calculated by solving a combined momentum equation. Free-stream boundary conditions are used at the inflow boundary as well as at the outer boundary. A symmetry boundary condition is imposed at the circumferential edges of the grid, while a simple extrapolation is used at the downstream boundary. A combination of symmetry and extrapolation boundary condition is used at the center line (axis). Since the free-stream flow is supersonic, a nonreflection boundary condition is used at the outer boundary. Similar boundary conditions are used for the segments.

3. MODEL GEOMETRY AND COMPUTATIONAL GRID

The primary or parent projectile is a 10-caliber (1 caliber = diameter at the cylindrical section) cone-cylinder-flare projectile. It consists of a 4.46-caliber conical nose, a 2.82-caliber cylindrical section, and a 3.0-caliber 12.2° flare. Figure 4 shows a computational grid for this case. It shows the projectile configuration and the surrounding grid which consists of approximately 20,000 grid

points. The grid in the wake region consists of 99 points in the streamwise direction and 119 points in the normal direction. The surface points for each region (body and wake) are selected using an interactive design program. Each grid section was obtained separately and then appended to provide the full grid. The grid for the body region, as well as the wake region, was obtained algebraically. An expanded view of the wake region grid is shown in Figure 5. The projectile afterbody seen here went through many design changes after the computations were completed. This resulted in the use of a slightly different afterbody in the test firings compared to the computational model afterbody. However, because of the relatively large size of the afterbody base compared to the segment, the effect of this change in the afterbody is expected to be minimal on the flow field over the segments. Figure 5 clearly shows the grid clustering near the base corner of the projectile. Another unique feature of this grid is that the dark band of grid points at the base corner (in the normal direction) slowly opens up with increasing distance downstream of the base. This is an effort to make good use of the grid points and place them in regions of large flow gradients such as the free shear layer in the wake region. The full grid is split into five zones--a small zone in front of the projectile, three zones on the projectile itself, and a wake zone.

The current problem of interest is the effect of the wake of the primary projectile on the small cylindrical body. Each cylindrical segment has a diameter of 9 mm and a length to diameter ratio (L/D) of 2. A typical body conforming grid for the segment is shown in Figure 6 and is overset onto the primary projectile grid. This corresponds to the matted position when the segment is positioned inside of the parent projectile with the aft end of the segment flush with the base of the parent projectile. The segment grid is generated easily independently of the major grid. It consists of 101 points in the streamwise direction and 31 points in the normal direction away from the body surface. The Chimera technique, as stated earlier, allows individual grids to be generated with any grid topology, thus making the grid generation process easier. For moving body problems, the segment grid, shown in Figure 6 in the matted position, moves with the segment as the segment separates from the parent projectile and moves downstream into the wake (see Figure 7). Again, there is no need to generate new grids for the segment and/or the parent projectile during the dynamic process.

4. RESULTS

Time-accurate calculations have been performed to numerically simulate the ejection and separation of the segments in the wake of a parent projectile. Numerical computations were performed for the cases where the parent projectile and one or two segments are in relative motion. All computations have been run at $M_\infty = 4.4$ and $\alpha = 0°$ and atmospheric flight conditions were used. The three-plane version of the 3-D code was run for the 0° angle of attack case and, therefore, all grids were rotated circumferentially 5° on either side of the mid-plane. This provided the three planes needed in the code to use central finite differences in the circumferential direction.

A converged result was first obtained for the parent projectile alone with the segment in the matted position. Unsteady computations were carried out for the 9-mm segments. In each of these runs, the solution was kept frozen in the first three zones and computations were made in zone 4 (a small zone upstream of the base), as well as all zones in the wake region only. The frozen solution in zone 3 provided upstream boundary conditions for zone 4. In each case with the segment, the solution was obtained in a time-accurate manner starting with the ejection of the segment into the wake or base region of the parent projectile. These calculations required 15M words of memory (total memory for all grid zones) and each case used about 60 hours of computer time on the Cray X-MP supercomputer.

A few qualitative results for the one-segment case and the two-segment case are presented, respectively. Figure 8 shows the Mach number contours for the parent projectile with the segment in the matted position. As expected, it shows the shock wave emanating from the nose of the projectile. A strong shock wave is also seen to originate from the cylinder-flare junction. The flow expands at the base corner which is followed by a recompression shock downstream of the base. As shown in the figure, the outer boundary is placed close to the projectile and a nonreflection boundary condition procedure is used. The shock waves and the expansion waves pass through this boundary rather smoothly.

Initial system design considerations provided the data used for the ejection velocity of the projectile segments. For the one segment case, the segment is ejected out from the parent projectile at 92.9 m/s. Figure 9 shows snapshots in time of the Mach number contours in the

10

base region for various locations of the segment in the wake. The first picture on the top of this figure corresponds to the case when the segment has just come out of the base of the parent projectile. The other three positions or locations correspond to separation distances (L) of about 2, 4, and 6 calibers from the base of the parent projectile. For L=2, the segment is completely immersed in the subsonic wake of the parent projectile. As seen in this figure, for L=4, the flow right in front of the segment is still subsonic. The flow becomes supersonic away from it in the normal direction and one can see the recompression shock which follows the flow expansions at the base of the parent projectile. As the separation distance is increased to L=6, the flow field ahead of the segment becomes supersonic. A bow shock wave forms ahead of the segment. As L is increased further, this bow shock wave becomes stronger. These changes in the flow structure change the pressure on the front face of the segment (stronger the shock, higher the pressure) and thus, the aerodynamic drag. The overall flow field behind the segment looks generally the same in all these cases and the pressure on the back face of the segment does not change significantly.

A set of range tests[7] have been performed for the multi-segment ejection case from the parent projectile. Various configurations with different length-to-diameter ratios and nose radii of the segment were included in the tests. The particular case for which numerical computations have been made corresponds to a L/D of 2 and nose radius of 0.5 caliber. Two segments have been numerically simulated. The ejection velocities for these two segments are 52 and 27 m/s for the first (first one to come out) and second segment, respectively. The initial conditions used in the numerical computations for ejection of these segments were obtained from the experimental test results. The second segment was ejected after the first segment was about 1.9 calibers away from the base of the parent projectile. The developed Chimera composite overset grid approach was used to numerically model this experimental, time-dependent separation process. Figure 10 shows the computed pressure contours for the entire configuration which includes the parent projectile and the two segments. It shows the instantaneous shock wave and the expansion waves structure when the segments are about 4 and 10 calibers away in the wake. Comparison of the computational results are made with the available experimental results. Figure 11 shows the computed pressure contours in the base region for the two-segment case compared with the experimentally obtained spark shadowgraphs. It corresponds to the case where the second segment is at a separation distance of about 1.25 calibers from the base of the parent projectile. At that time, the first segment is at a separation distance of about 3.8 calibers. As seen in the

11

figure, these locations agree well with the experimental test results. Although not shown here, similar comparisons have also been made for other segment positions further downstream in the wake indicating good agreement between the computed and experimental results.

The entire flow field over the projectile, including the segment, is computed to obtain the desired aerodynamics. Surface pressures, including the base pressures and the viscous stresses, are known from the computed flow field and can be integrated to give the aerodynamic drag for both parent projectile as well as the cylindrical segments. The drag coefficient for the segments is shown in Figure 12 as a function of the separation distance. This drag coefficient is based on the area of the segment and the free-stream dynamic pressure. As mentioned earlier, for small separation distances (L<2), the segment is submerged in the subsonic wake of the parent projectile. The pressure behind the segment is higher than the pressure ahead of the segment and, therefore, results in negative drag. As L is increased, the approaching flow to the segment becomes supersonic and a bow shock wave forms in front of the segment. This increases the pressure at the front face of the segment and results in higher drag. Figure 12 also shows the increase in drag with increasing separation distance. Also included here are the previously computed[5] quasi-static results obtained for a few locations of the segment in the wake of the parent projectile. These calculations do not take into account the relative motion between the parent body and the segment. As seen in this figure, there is a substantial difference in the predicted drag between the static and the dynamic cases with the drag being lower for the dynamic case. This highlights the need for time-dependent dynamic solution techniques to accurately simulate problems involving multiple bodies in relative motion. The drag for the first segment (first one to come out) is shown in solid line. For the first two calibers of separation distance, both segments essentially follow the same curve. However, for L > 2.5, the drag of the first segment is found to be lower than that of the second segment since it is in the wake of the second segment. Although not shown here, the drag for the parent projectile changes very little in the presence of the small cylindrical segments.

Figures 13 and 14 show the separation distance and the segment velocity as a function of time, respectively. The computed result for the first segment is shown by the solid line and that of the second one by a dashed line. The second segment is ejected about 1.2 ms after the first one. As shown in Figure 13, the separation distance for the initial matted position of the segments is -0.3 calibers. The computed locations of the segments agree fairly well with the

12

experimentally observed results. Figure 14 shows the comparison of the computed segment velocity (relative to the parent projectile) with the data. For the first 2 msec, the segment velocity for the first segment decreases slightly and then increases from thereon with time. The segment velocity for the second segment decreases only slightly during this time duration. Again, this trend is seen in the experimental results as well.

5. CONCLUDING REMARKS

A computational study has been undertaken to compute the aerodynamics of small cylindrical segments being ejected into the wake of a parent projectile. Flow field computations have been performed at a supersonic Mach number, M_∞ = 4.4 and α =0.0° using an unsteady, zonal F3D, Navier-Stokes code and the Chimera composite grid discretization technique. The computed results show the qualitative features of the base region flow field for the parent projectile for both the matted position and other positions of the segment in the wake. The predicted flow field over the small segments was found to undergo significant changes as the segments separated from the parent projectile. For small separation distances (L<2), the segment experiences negative drag for the dynamic case. With increasing separation distance, a bow shock was found to form in front of the segment resulting in higher drag. A significant difference in the predicted drag was observed between the quasi-steady and the dynamic simulations. The time-dependent computations were shown to be essential for problems involving relative motion. Comparison of the computed results for the two-segments case have been made with the available experimental results and computed locations, separation distances, and segment velocities were found to be in very good agreement with the experimental results.

This work represents a major advance in capability for determining the aerodynamics of multiple-body configurations. The coupling of the fluid dynamic solution and rigid-body motion is a major advance and significant accomplishment that eliminates the need for simplifying assumptions and allows more accurate physically based simulations. Together with increased computational resources and the advanced technologies described in this report, multiple design configurations can be accurately simulated with a "best" design being chosen more quickly.

13
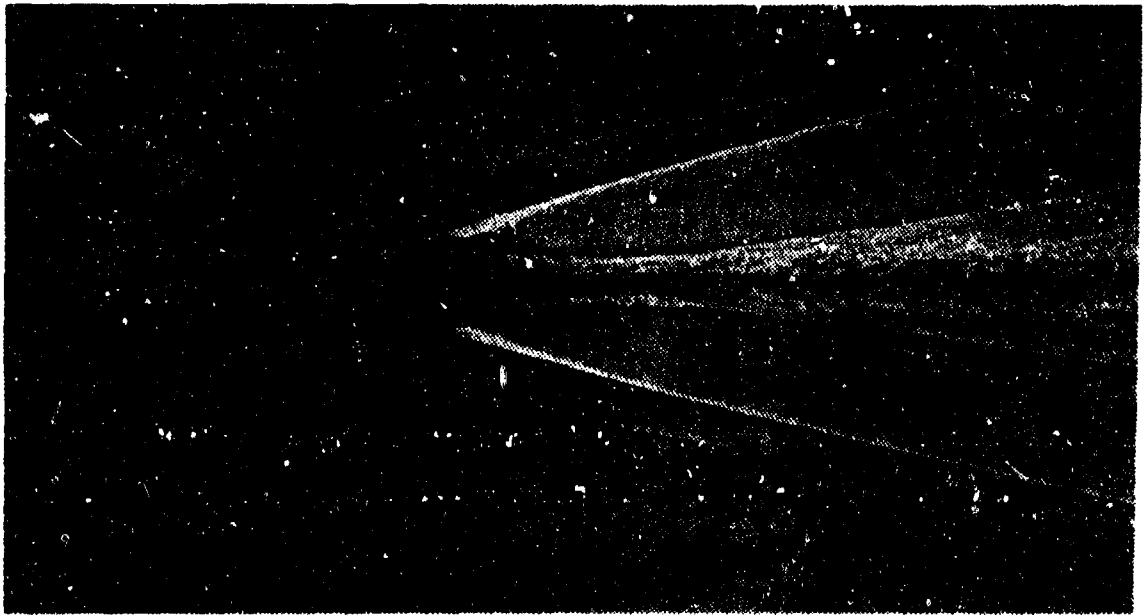
Figure 1. <u>Spark Shadowgraph for Multiple Segments in Wake of the Parent Projectile.</u>

PARENT(MAJOR) DOMAIN

ARTIFICIAL BOUNDARY IN
PARENT DOMAIN

SEGMENT(MINOR) DOMAIN

Figure 2. Intergrid Communication.

SEGMENT BC CONDITION
INTERPOLATED FROM
PARENT GRID

PARENT GRID

SURFACE IN SEGMENT GRID
THAT CREATES HOLE IN PARENT
GRID

HOLE BOUNDARY IN
PARENT GRID

PARENT BC INTERPOLATED
FROM SEGMENT GRID

OVERLAP REGION

Figure 3. Overlap Region Between Grids.

15

Figure 4. Computational Grid for the Parent Projectile (Major Grid).
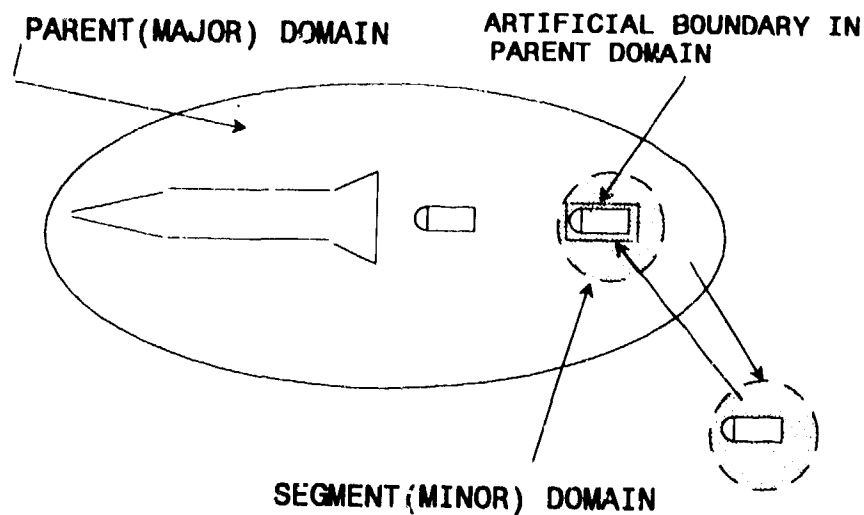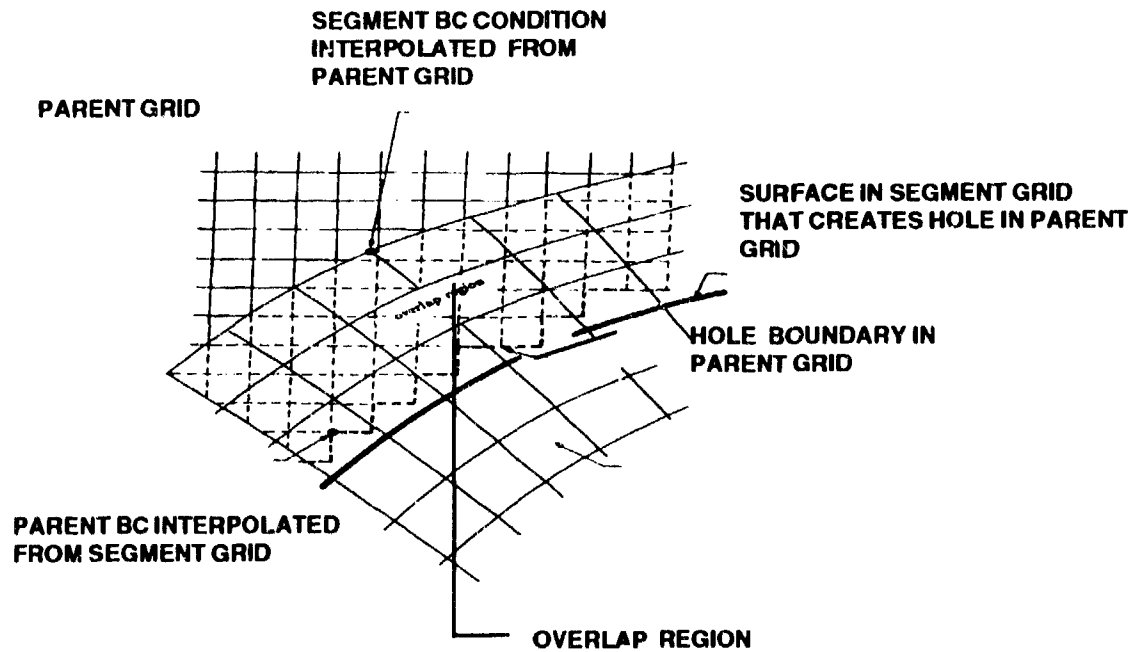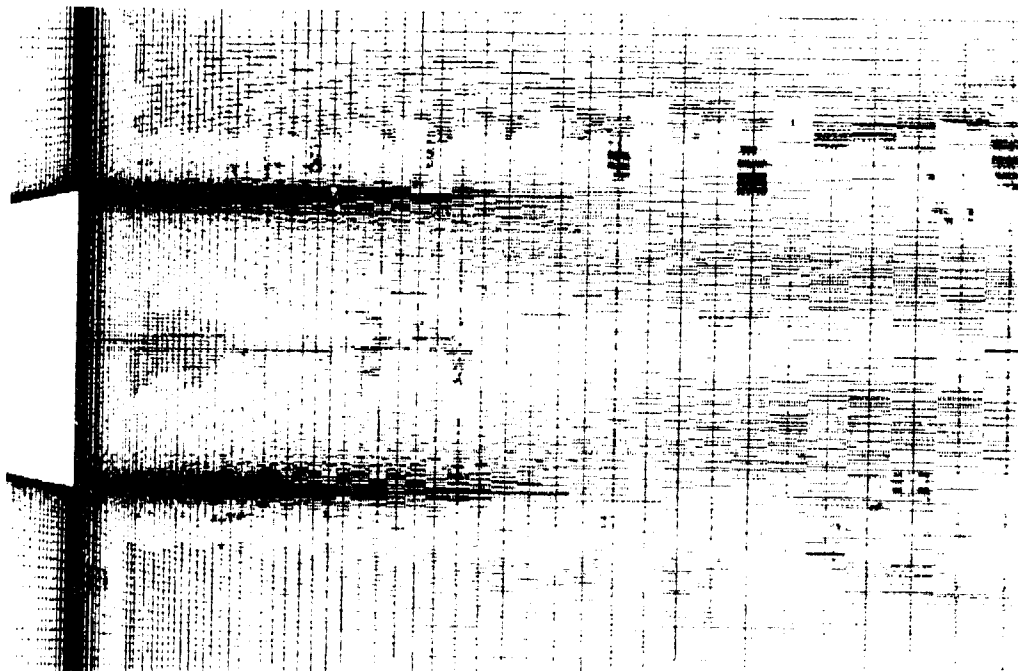

Figure 5. Expanded View of the Base Region Grid.

17

The following page intentionally left blank.
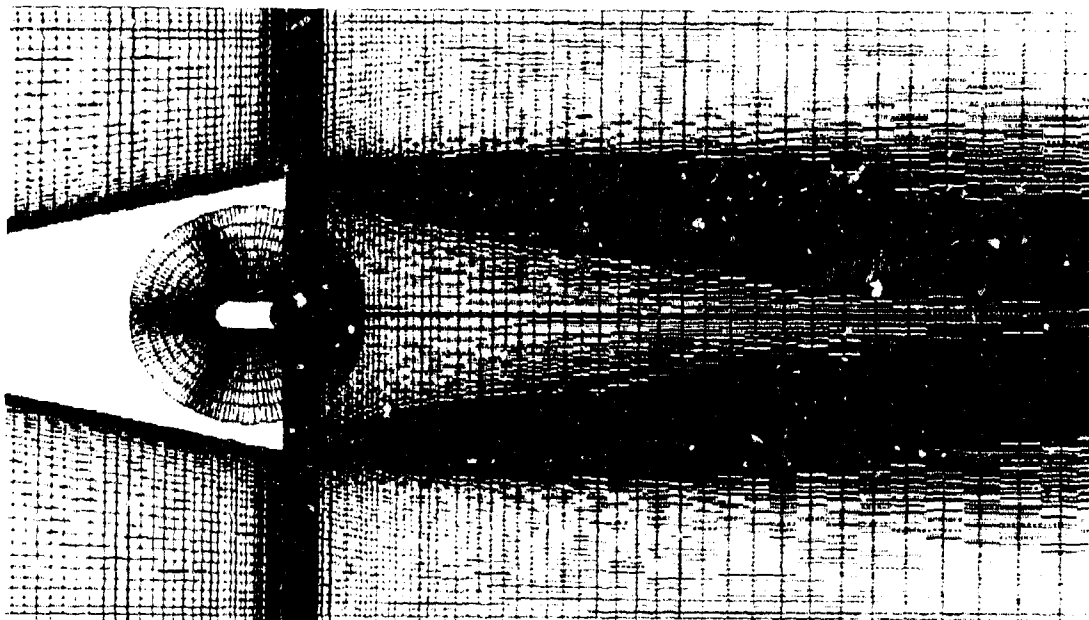
Figure 6. Segment Grid (Minor Grid) in Matted Position.
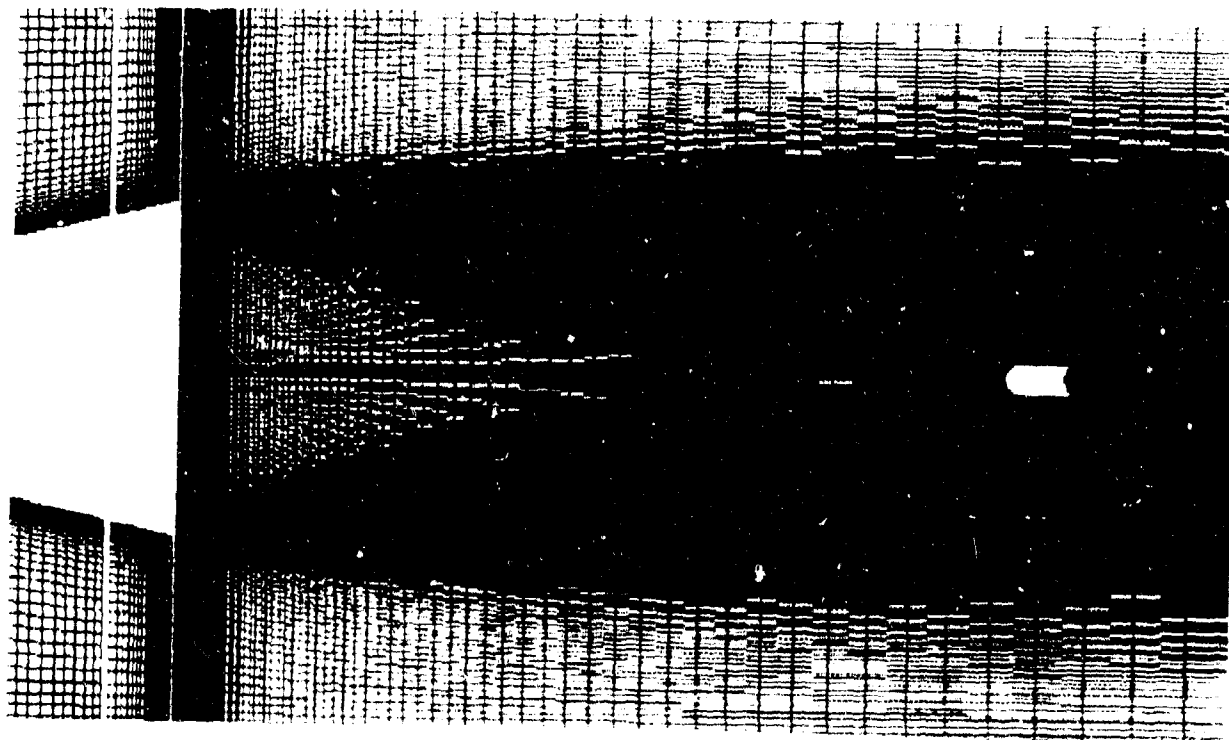
Figure 7 Segment Grid With the Segment in Wake of the Parent Projectile.

19

Figure 8. Mach Contours, M_∞ = 4.4, α = 0, Segment in Matted Position.
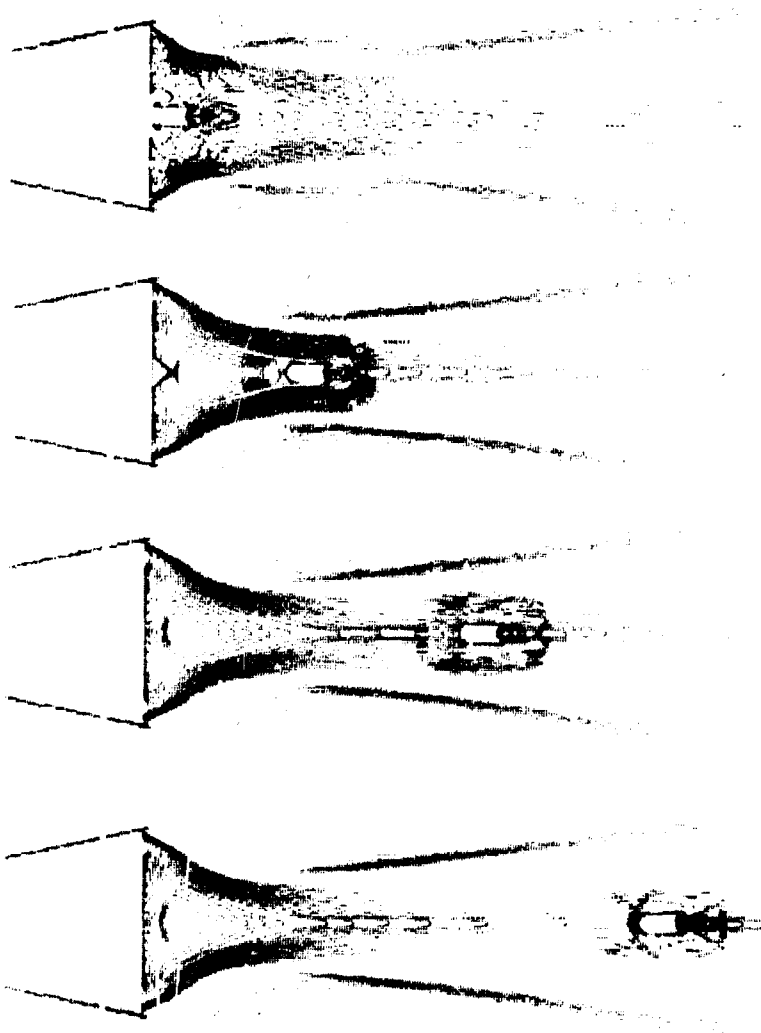
Figure 9. Mach Contours, M_∞ = 4.4, α = 0, Segment in Various Locations in the Wake.

21

The following page intentionally left blank.
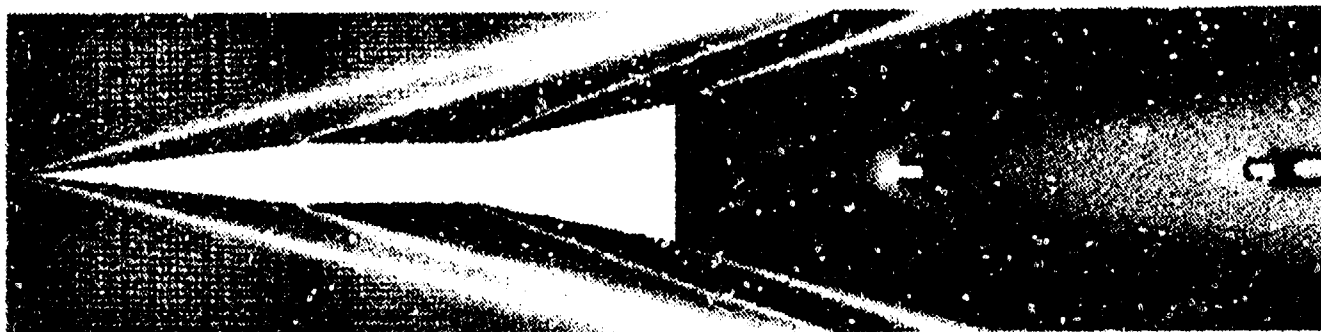
Figure 10. Computed Pressure Contours for the Entire System, $M_\infty = 4.4$, $\alpha = 0$.
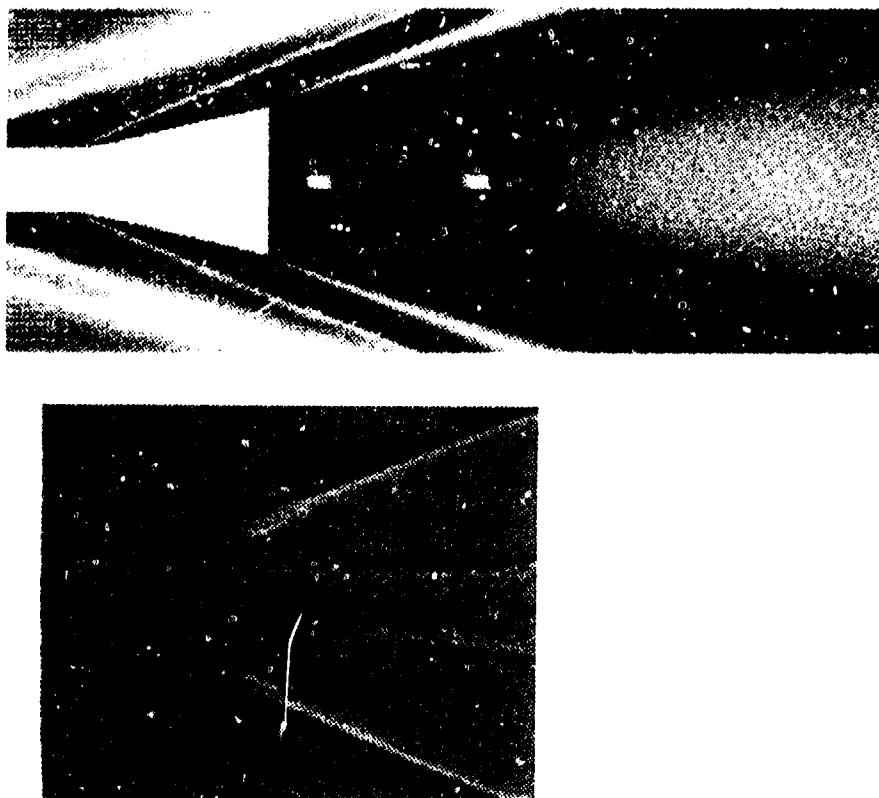
Figure 11. Comparison of Computed Pressure Contours With Spark Shadowgraph, $M_\infty = 4.4$, $\alpha = 0$.

The following page intentionally left blank
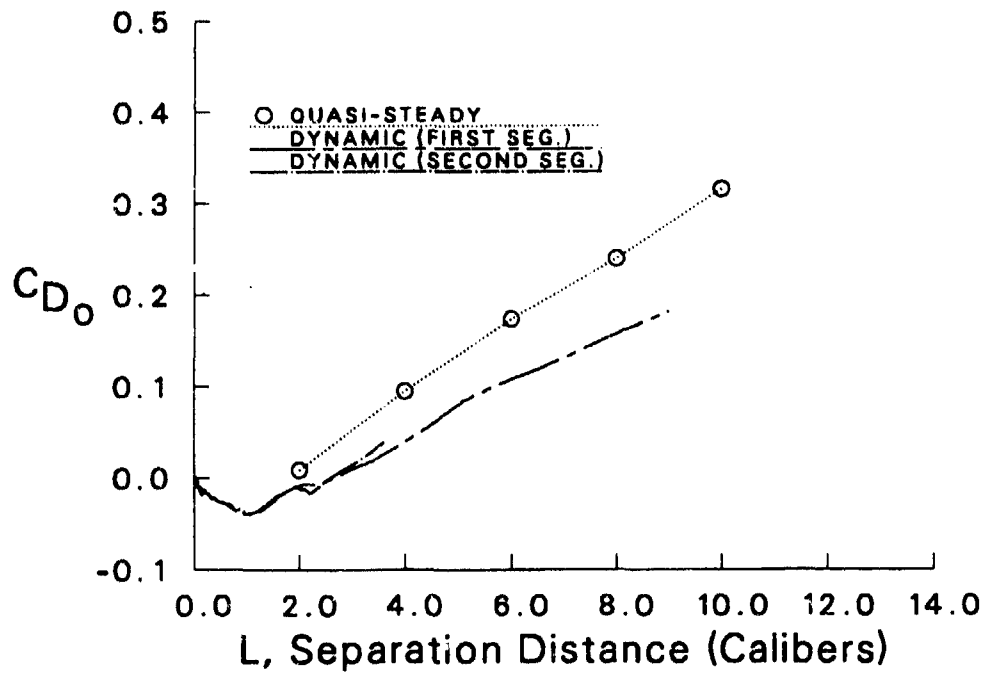
Figure 12. Drag Coefficient, M_ = 4.4, α = 0 (Static and Dynamic).
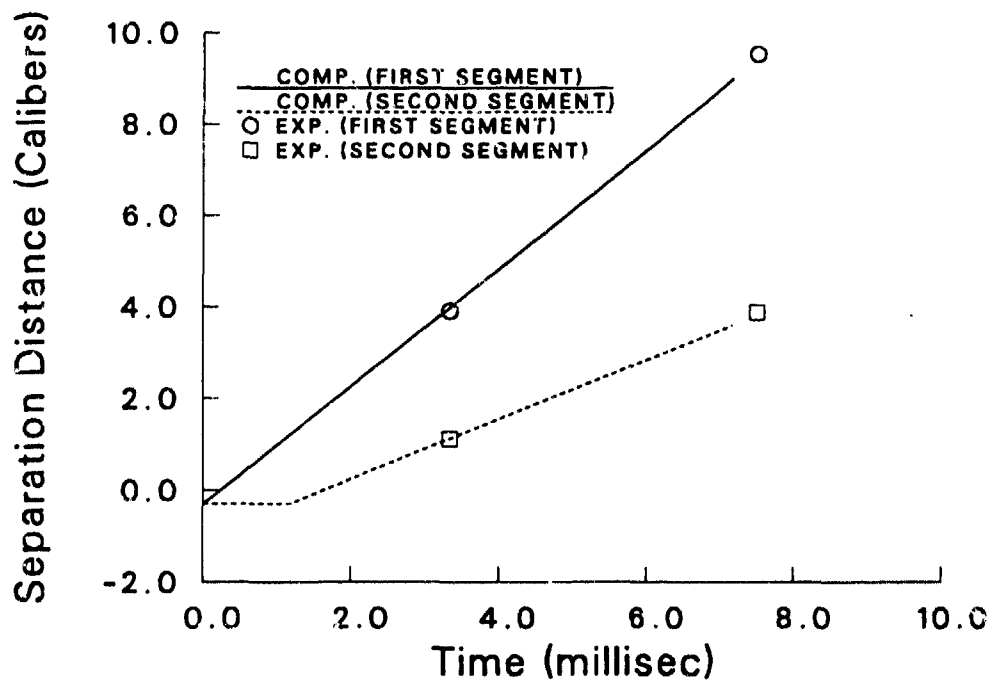
Figure 13. Separation Distance vs Time, M_ = 4.4, α = 0 (Dynamic).
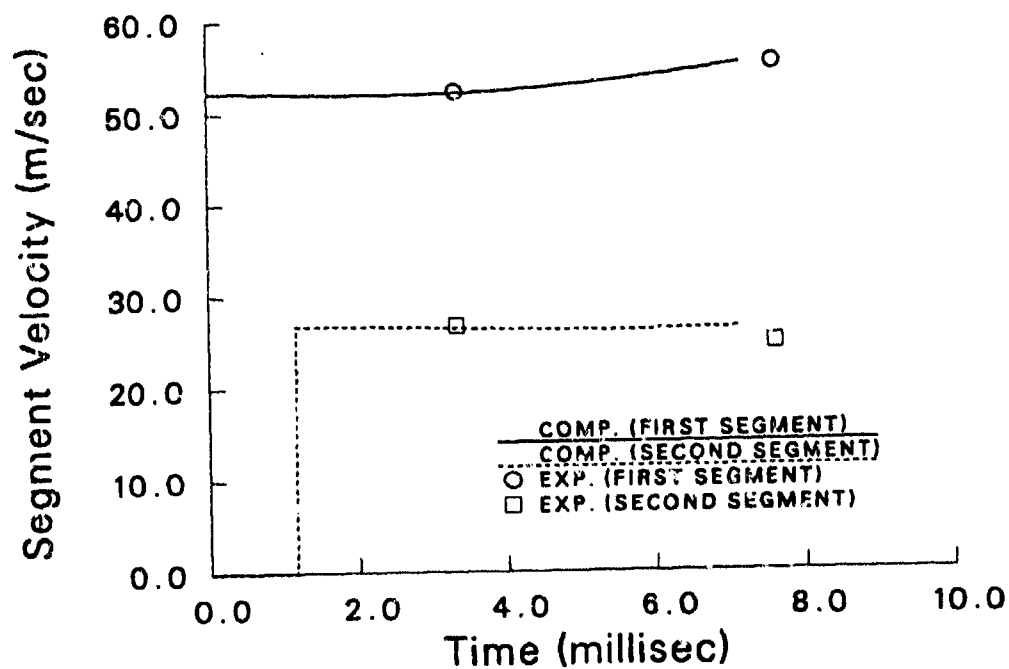
Figure 14.   Segment Velocity vs Time,   M_ = 4.4, α = 0 (Dynamic).

6. REFERENCES

1. Sahu, J., C. J. Nietubicz, and J. L. Steger. "Navier-Stokes Computations of Projectile Base Flow With and Without Base Injection." BRL-TR-02532, U.S. Army Ballistic Research Laboratory, Aberdeen Proving Ground, MD, November 1983 (also see AIAA Journal, vol. 23, no. 9, pp. 1348–1355, September 1985).

2. Sahu, J. "Supersonic Base Flow Over Cylindrical Afterbodies With Base Bleed." AIAA Paper No. 86-0487, Proceedings of the 24th Annual Aerospace Sciences Meeting, Reno, NV, January 1986.

3. Sahu, J. "Computations of Supersonic Flow Over a Missile Afterbody Containing an Exhaust Jet." AIAA Journal of Spacecraft and Rockets, vol. 24, no. 5, pp. 403–410, September-October 1987.

4. Sahu, J., and J. L. Steger. "Numerical Simulation of Three-Dimensional Transonic Flows." AIAA Paper No. 87-2293, Atmospheric Flight Mechanics Conference, Monterey, CA, August 1987 (also see BRL-TR-2903, March 1988).

5. Sahu, J. "Numerical Computations of Transonic Critical Aerodynamic Behavior." AIAA Journal, vol. 28, no. 5, pp. 807-816, May 1990 (also see BRL-TR-2962, December 1988).

6. Sahu, J., and C. J. Nietubicz. "Three Dimensional Flow Calculation for a Projectile With Standard and Dome Bases." BRL-TR-3150, U.S. Army Ballistic Research Laboratory, Aberdeen Proving Ground, MD, September 1990.

7. Von Wahlde, R. Private Communications, Army Research Laboratory.

8. Sahu, J. , and C.J. Nietubicz. "A Computational Study of Cylindrical Segments in the Wake of a Projectile." BRL-TR-3254, U.S. Army Ballistic Research Laboratory, Aberdeen Proving Ground, MD, August 1991.

9. Steger, J.L., F.C. Dougherty, and J.A. Benek. "A Chimera Grid Scheme." Advances in Grid Generation, K.N. Ghia and U. Ghia, eds., ASME FED-5, June 1983.

10. Atta, E.H., and J. Vadyak. "A Grid Interfacing Zonal Algorithm for Three-Dimensional Flow Transonic Flows about Aircraft Configurations." AIAA Paper No. 82-1017, 1982.

11. Benek J.A., T.L. Donegan, and N.E. Suhs. "Extended Chimera Grid Embedding Scheme with Application to Viscous Flows." AIAA Paper No. 87-1126-CP, 1987.

12. Buning, P.G., I.T. Chiu, S. Obayashi, Y.M. Rizk, and J.L. Steger. "Numerical Simulation of the Integrated Space Shuttle Vehicle in Ascent." AIAA Atmospheric Flight Mechanics Conference, August 15-17, 1988.

13. Meakin, R.L., and N. Suhs. "Unsteady Aerodynamic Simulation of Multiple Bodies in Relative Motion." AIAA 9th Computational Fluid Dynamics Conference, AIAA Paper No. 89-1996, June 1989.

14. Pulliam, T. H., and J. L. Steger. "On Implicit Finite-Difference Simulations of Three-Dimensional Flow." AIAA Journal, vol. 18, no. 2, pp. 159-167, February 1982.

15. Baldwin, B. S., and H. Lomax. "Thin Layer Approximation and Algebraic Model for Separated Turbulent Flows." AIAA Paper No. 78-257, January 1978.

16. Steger, J.L., S.X. Ying, and L.B. Schiff. "A Partially Flux-Split Algorithm for Numerical Simulation of Compressible Inviscid and Viscous Flows." Proceedings of the Workshop on Computational Fluid Dynamics, Institute of Nonlinear Sciences, U. of California, Davis, CA, 1986.

2	Administrator Defense Technical Info Center ATTN: DTIC-DDA Cameron Station Alexandria, VA 22304-6145		1	Commander U.S. Army Missile Command ATTN: AMSMI-RD-CS-R (DOC) Redstone Arsenal, AL 35898-5010
1	Commander U.S. Army Materiel Command ATTN: AMCAM 5001 Eisenhower Ave. Alexandria, VA 22333-0001		1	Commander U.S. Army Tank-Automotive Command ATTN: AMSTA-JSK (Armor Eng. Br.) Warren, MI 48397-5000
1	Director U.S. Army Research Laboratory ATTN: AMSRL-OP-SD-TA, Records Management 2800 Powder Mill Rd. Adelphi, MD 20783-1145		1	Director U.S. Army TRADOC Analysis Command ATTN: ATRC-WSR White Sands Missile Range, NM 88002-5502
3	Director U.S. Army Research Laboratory ATTN: AMSRL-OP-SD-TL, Technical Library 2800 Powder Mill Rd. Adelphi, MD 20783-1145		1	Commandant U.S. Army Infantry School ATTN: ATSH-WCB-O Fort Benning, GA 31905-5000

Aberdeen Proving Ground

1	Director
	U.S. Army Research Laboratory
	ATTN: AMSRL-OP-SD-TP,
	          Technical Publishing Branch
	2800 Powder Mill Rd.
	Adelphi, MD 20783-1145
			2	Dir, USAMSAA
				ATTN: AMXSY-D
				          AMXSY-MP, H. Cohen

2	Commander U.S. Army Armament Research, Development, and Engineering Center ATTN: SMCAR-TDC Picatinny Arsenal, NJ 07806-5000		1	Cdr, USATECOM ATTN: AMSTE-TC
			1	Dir, USAERDEC ATTN: SCBRD-RT
1	Director Benet Weapons Laboratory U.S. Army Armament Research, Development, and Engineering Center ATTN: SMCAR-CCB-TL Watervliet, NY 12189-4050		1	Cdr, USACBDCOM ATTN: AMSCB-CII
			1	Dir, USARL ATTN: AMSRL-SL-I
1	Director U.S. Army Advanced Systems Research and Analysis Office (ATCOM) ATTN: AMSAT-R-NR, M/S 219-1 Ames Research Center Moffett Field, CA 94035-1000		5	Dir, USARL ATTN: AMSRL-OP-AP-L

1   HQDA (SARD-TR/Ms. K. Kominos)
    WASH DC 20310-0103

1   HQDA (SARD-TR/Dr. R. Chait)
    WASH DC 20310-0103

5   Commander
    U.S. Army Armament Research,
        Development, and Engineering Center
    ATTN: SMCAR-AET-A,
                H. Hudgins
                S. Kahn
                J. Grau
                C. Ng
                W. Koenig
    Picatinny Arsenal, NJ 07806-5000

1   Commander
    U.S. Army Armament Research,
        Development, and Engineering Center
    ATTN: SFAE-FAS-SD, M. Devine
    Bldg. 171
    Picatinny Arsenal, NJ 07806-5000

1   Commander
    U.S. Army Missile Command
    ATTN: AMSMI-RD-SS-AT, B. Walker
    Redstone Arsenal, AL 35898-5010

1   Commander
    U.S. Naval Surface Warfare Center
    Dahlgren Division
    ATTN: Dr. F. Moore
    Dahlgren, VA 22448

3   Commander
    Naval Surface Warfare Center
    ATTN: Code R44,
                Dr. F. Priolo
                Dr. A. Wardlaw
            K24, B402-12, Dr. W. Yanta
    White Oak Laboratory
    Silver Spring, MD 20903-5000

3   Air Force Armament Laboratory
    ATTN: AFATL/FXA,
                Dr. L. B. Simpson
                Dr. David Belk
                Dr. G. Abate
    Eglin AFB, FL 32542-5434

1   USAF Wright Aeronautical Laboratories
    ATTN: AFWAL/FIMG, Dr. J. Shang
    WPAFB, OH 45433-8553

3   Director
    National Aeronautics and Space Administration
    Langley Research Center
    ATTN: Tech Library
                Dr. M. J. Hemsch
                Dr. J. Smith
    Langley Station
    Hampton, VA 23665

3   Director
    National Aeronautics and Space Administration
    Ames Research Center
    ATTN: MS-227-8, L. Schiff
                MS-258-1,
                    T. Holst
                    D. Chaussee
    Moffett Field, CA 94035

1   Massachusetts Institute of Technology
    ATTN: Technical Library
    77 Massachusetts Ave.
    Cambridge, MA 02139

2   Director
    Sandia National Laboratories
    ATTN: Dr. W. Oberkampf
                Dr. F. Blottner
    Division 1554
    P.O. Box 5800
    Albuquerque, NM 87185

2   VRA Inc.
    ATTN: Dr. C. Lewis
                Dr. B. A. Bhutta
    P.O. Box 50
    Blacksburg, VA 24060

1   Science Applications, Inc.
    Computational Fluid Dynamics Division
    ATTN: Dr. D. W. Hall
    994 Old Eagle School Road
    Suite 1018
    Wayne, PA 19087

30

6	Alliant Techsystems, Inc. ATTN: J. Bode C. Candland L. Osgood R. Buretta R. Becker M. Swenson 600 Second St. NE Hopkins, MN 55343
1	McDonnell Douglas Missile Systems Co. ATTN: F. McCotter Mailcode 306-4249 P.O. Box 516 St. Louis, MO 63166-0516
2	Institute of Advanced Technology ATTN: Dr. T. Kiehne Dr. W. G. Reineke 4030-2 W. Baker Lane Austin, TX 78759
1	University of California, Davis Department of Mechanical Engineering ATTN: Prof. H. A. Dwyer Davis, CA 95616
1	University of Maryland Department of Aerospace Engineering ATTN: Dr. J. D. Anderson, Jr. College Park, MD 20742
1	University of Texas Department of Aerospace Engineering and Engineering Mechanics ATTN: Dr. D. S. Dolling Austin, TX 78712-1055
1	University of Florida Department of Engineering Sciences College of Engineering ATTN: Prof. C. C. Hsu Gainesville, FL 32611
1	Pennsylvania State University Department of Mechanical Engineering ATTN: Dr. Kenneth Kuo University Park, PA 16802

1	Florida Atlantic University Department of Mechanical Engineering ATTN: Dr. W. L. Chow Boca Raton, FL 33431
1	North Carolina State University Department of Mechanical and Aerospace Engineering ATTN: Prof. D. S. McRae Box 7910 Raleigh, NC 27695-7910
1	Georgia Institute of Technology School of Aerospace Engineering ATTN: Dr. Warren C. Strahle Atlanta, GA 30332
2	University of Illinois at Urbana-Champaign Department of Mechanical and Industrial Engineering ATTN: Prof. A. L. Addy Prof. Craig Dutton 114 Mechanical Engineering Building 1206 West Green Street Urbana, IL 61801
1	Scientific Research Associates ATTN: Dr. Richard Buggeln 50 Nye Road P.O. Box 1058 Glastonbury, CT 06033
1	AEDC Calspan Field Service ATTN: Dr. John Benek MS 600 Tullahoma, TN 37389
1	Visual Computing ATTN: Jeffrey Q. Cordova 883 N. Shoreline Blvd. Suite B210 Mountain View, CA 94043
1	MDA Engineering, Inc. ATTN: John P. Steinbrenner 500 E. Border St. Suite 401 Arlington, TX 76010

1	Climate Control Division Product Engineering Office ATTN: Tom Gielda 15031 South Commerce Dr. Dearborn, MI 48120		**Aberdeen Proving Ground**
		25	Dir, USARL ATTN: AMSRL-WT-P, Mr. Albert Horst AMSRL-WT-PB, Dr. E. Schmidt Dr. M. Bundy
1	Carrier Corporation ATTN: Howard Gibeling P.O. Box 4808 Carrier Parkway Syracuse, NY 13221		Dr. K. Fansler Mr. E. Ferry Mr. B. Guidos Mrs. K. Heavey Mr. H. Edge
1	NASA Marshall Space Flight Control Center ATTN: Kevin Tucker Mail Stop ED-32 Huntsville, AL 35812		Dr. G. Cooper Mr. V. Oskay Dr. P. Plostins Dr. A. Mikhail Dr. J. Sahu
1	Aerojet Electronics Plant ATTN: Dr. Dan Pillasch Bldg. 170/Dept. 5311 P.O. Box 296 Azusa, CA 91702		Mr. P. Weinacht AMSRL-WT, Dr. A. Barrows AMSRL-WT-PD, Dr. B. Burns AMSRL-WT-PA, Dr. T. Minor Mr. M. Nusca AMSRL-WT-W, Dr. C. Murphy AMSRL-WT-WB, Dr. W. D'Amico AMSRL-WT-NC, Ms. D. Hisley Mr. R. Lottero AMSRL-CI-C, Dr. W. Sturek Dr. N. Patel AMSRL-CI-AD, Mr. C. Nietubicz
		2	Cdr, USAARDEC ATTN: Firing Tables, Bldg 120, Mr. R. Lieske Mr. R. McCoy

USER EVALUATION SHEET/CHANGE OF ADDRESS

This Laboratory undertakes a continuing effort to improve the quality of the reports it publishes. Your comments/answers to the items/questions below will aid us in our efforts.

1. ARL Report Number ___ARL-TR-590_____ Date of Report ___October 1994____

2. Date Report Received _____

3. Does this report satisfy a need? (Comment on purpose, related project, or other area of interest for which the report will be used.) _____

_____

_____

4. Specifically, how is the report being used? (Information source, design data, procedure, source of ideas, etc.)_____

_____

_____

5. Has the information in this report led to any quantitative savings as far as man-hours or dollars saved, operating costs avoided, or efficiencies achieved, etc? If so, please elaborate. _____

_____

_____

6. General Comments. What do you think should be changed to improve future reports? (Indicate changes to organization, technical content, format, etc.) _____

_____

_____

_____

_____
Organization
_____
CURRENT   Name
ADDRESS
_____
Street or P.O. Box No.
_____
City, State, Zip Code

7. If indicating a Change of Address or Address Correction, please provide the Current or Correct address above and the Old or Incorrect address below.

_____
Organization
_____
OLD   Name
ADDRESS
_____
Street or P.O. Box No.
_____
City, State, Zip Code

(Remove this sheet, fold as indicated, tape closed, and mail.)
(DO NOT STAPLE)